Current-Induced Polarization and the Spin Hall Effect at Room Temperature

N. P. Stern,[1] S. Ghosh,[1] G. Xiang,[2] M. Zhu,[2] N. Samarth,[2] and D. D. Awschalom[1,*]

[1]*Center for Spintronics and Quantum Computation, University of California, Santa Barbara, California 93106, USA*
[2]*Department of Physics, Pennsylvania State University, University Park, Pennsylvania 16802, USA*

(Received 11 July 2006; published 20 September 2006)

Electrically induced electron spin polarization is imaged in *n*-type ZnSe epilayers using Kerr rotation spectroscopy. Despite no evidence for an electrically induced internal magnetic field, current-induced in-plane spin polarization is observed with characteristic spin lifetimes that decrease with doping density. The spin Hall effect is also observed, indicated by an electrically induced out-of-plane spin polarization with opposite sign for spins accumulating on opposite edges of the sample. The spin Hall conductivity is estimated as $3 \pm 1.5\ \Omega^{-1}\,\mathrm{m}^{-1}/|e|$ at 20 K, which is consistent with the extrinsic mechanism. Both the current-induced spin polarization and the spin Hall effect are observed at temperatures from 10 to 295 K.

DOI: 10.1103/PhysRevLett.97.126603 PACS numbers: 72.25.Hg, 71.70.Ej, 78.47.+p, 85.75.−d

The ability to manipulate carrier spins in semiconductors through the spin-orbit (SO) interaction is one of the primary motivations behind the field of spintronics. SO coupling provides a mechanism for the generation and manipulation of spins solely through electric fields [1–3], obviating the need for applied magnetic fields. Much of the recent interest in the consequences of SO coupling in semiconductors surrounds the production of a transverse spin current from an electric current, known as the spin Hall effect. Though predicted three decades ago [4], the first experimental observations of the spin Hall effect have appeared only recently [5–7]. Subsequent work on the spin Hall effect has addressed the importance of extrinsic or intrinsic mechanisms of the spin Hall conductivity [7–10], the nature of spin currents [11,12], and the potential ability both to produce and to detect spin Hall currents using only electric fields [13,14].

Previous experiments showing electrical generation of spin polarization in semiconductors through SO coupling have been performed at cryogenic temperatures in GaAs, the archetypical III–V zinc blende semiconductor. In contrast, the wide band gap and long spin coherence times of II–VI semiconductors allow many spin-related effects to persist to higher temperatures than typically observed in the GaAs system [15]. Many of the effects of SO coupling on the electrical manipulation of spin polarization have not been studied in detail in these compounds. In ZnSe, the extrinsic SO parameter $\lambda_{\mathrm{ZnSe}} = 1.06\ e\,\text{Å}^2$, as calculated from an extended Kane model, is 5 times less than that in GaAs, with $\lambda_{\mathrm{GaAs}} = 5.21\ e\,\text{Å}^2$ [10,16]. Despite weaker SO coupling, large extrinsic SO skew scattering has been observed in the anomalous Hall effect in magnetically doped ZnSe [17]. In this Letter, we optically measure electrically induced spin polarization in ZnSe epilayers that persists to room temperature. We observe in-plane current-induced spin polarization (CISP) in ZnSe with *n* doping ranging over 2 orders of magnitude and out-of-plane electrically induced spin accumulation at the edges of an etched channel, providing evidence for the extrinsic spin Hall effect. Unlike in previous studies of CISP and the spin Hall effect, both phenomena are measured at 300 K, demonstrating the electrical generation and routing of spins in semiconductors at room temperature.

A series of 1.5 μm thick *n*-type Cl-doped ZnSe epilayer samples with room temperature carrier concentrations $n = 5 \times 10^{16}$, 9×10^{17}, and $9 \times 10^{18}\ \mathrm{cm}^{-3}$ are grown by molecular-beam epitaxy (MBE) on semi-insulating (001) GaAs substrates. Perpendicular channels of width $w = 100\ \mu$m and length $l = 235\ \mu$m are patterned along the [110] and [1$\bar{1}$0] directions of the ZnSe epilayers, allowing an electric field E to be applied along both of the crystal axes. A voltage is applied across the device, with the effective E calculated from the measured temperature-dependent resistivity and current to eliminate the effect of contact resistance.

The samples are mounted in the variable temperature insert of a magneto-optical cryostat. Kerr rotation (KR) is measured in the Voigt geometry, with an in-plane applied magnetic field B perpendicular to the laser propagation direction [Fig. 1(a)]. 150-fs pulses from a 76-MHz mode-locked Ti:sapphire laser are frequency doubled and split into a circularly polarized pump and a linearly polarized probe beam with powers of 1.2 mW and 400 μW, respectively. The Kerr rotation angle θ_K of the polarization axis of the reflected probe beam measures the projection of electron spin polarization along the propagation direction [18]. Time-resolved KR measurements have found the electron g factor to be $g = 1.1$ and the spin coherence time to decrease with increasing n doping, with spin coherence times of 50, 20, and 0.5 ns for the $n = 5 \times 10^{16}$, 9×10^{17}, and $9 \times 10^{18}\ \mathrm{cm}^{-3}$ samples, respectively, at $T = 5$ K and $B = 0$ T [19].

In order to characterize the response of electron spins in ZnSe to applied electric fields, we perform spatially resolved KR measurements. In this pump-probe technique, the beams are normally incident on the sample and focused to a 15 μm spot [Fig. 1(c) inset]. The relative separation (d) of the pump and probe is varied in the direction of the

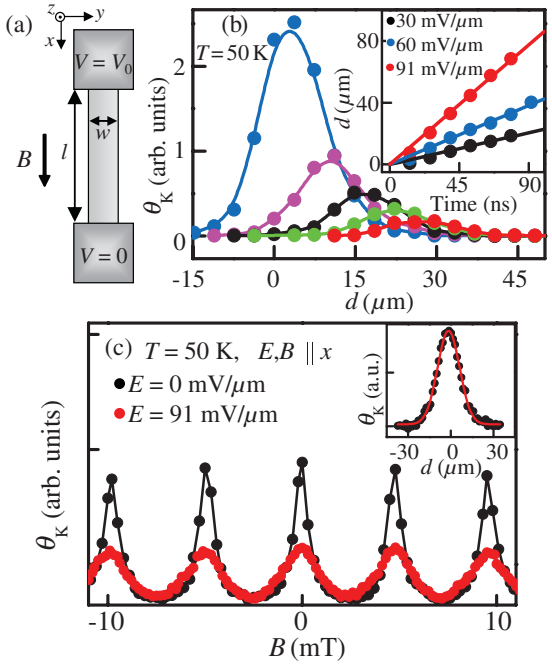

FIG. 1 (color). (a) Schematic of the device geometry for spin drag and CISP measurement. $B \parallel E$ and the probe beam is incident along $-z$. (b) Spatial profiles of the optically injected spin packet extracted from Fourier transforms of $\theta_K(B)$ at $E = 60$ mV/μm [20] for $\Delta t = 13.1$ ns (blue), $\Delta t = 26.2$ ns (magenta), $\Delta t = 39.3$ ns (black), $\Delta t = 52.4$ ns (green), and $\Delta t = 65.5$ ns (red). Gaussian fits at each laser repetition ($\Delta t = 13.1$ ns) give the center position of the packet as a function of time (inset). (c) KR from the $n = 5 \times 10^{16}$ cm^{-3} sample at $E = 0$ mV/μm (black) and $E = 91$ mV/μm (red). The KR peaks remain centered at $B = 0$, showing no evidence of B_{int}. The inset shows the Gaussian spatial profile of the optically injected spin packet, with a width of 15.5 μm.

electric field, and the KR of the probe measures the electron spin polarization injected by the pump along the z axis. Figure 1(b) follows the optically injected spin packet as it is dragged along the channel by a dc electric field of 60 mV/μm in the $n = 5 \times 10^{16}$ cm^{-3} sample. Extracting the drift velocity from the center of the Gaussian spin packets allows an estimate of the spin mobility of $\mu_s = 89 \pm 14$ cm^2/V s. This is 20 times less than that measured in GaAs [20] and over an order of magnitude smaller than the ZnSe electron mobility $\mu_e = 1440$ cm^2/V s at $T = 50$ K for this sample.

Experiments in GaAs have shown that an internal magnetic field B_{int} acts on electrons accelerated by an electric field, which has been attributed to inversion asymmetry [2,20–22]. KR as a function of B with fixed spatial ($d = 0$) and temporal (13.1 ns) pump-probe separation is shown in Fig. 1(c). This signal is periodic in B and symmetric about $B = 0$, making it a very sensitive probe for detecting B_{int} [2,20]. The KR signal remains centered at $B = 0$ as we increase E, showing no evidence of a B_{int} in the $n = 5 \times 10^{16}$ cm^{-3} and $n = 9 \times 10^{17}$ cm^{-3} samples along either the [110] or the [1$\bar{1}$0] channel. The spin coherence time of the $n = 9 \times 10^{18}$ cm^{-3} sample is too short to observe KR at 13.1 ns temporal separation, but no evidence of electrically induced spin precession from a B_{int} is observed using time-resolved KR with $B = 0$ [2]. These measurements provide an upper bound for the internal magnetic field of 0.1 mT with $E = 91$ mV/μm. The lack of any observable B_{int} in ZnSe can be attributed to the weaker spin-orbit coupling in ZnSe and the minimal strain in the epilayers.

For optical detection of CISP, we block the pump and measure static KR with probe energy tuned near the maximum of the KR signal, typically around 2.8 eV at 50 K. The KR is detected with a lock-in synchronized to a 2-kHz applied square wave electric field E. Typical magnetic field sweeps of KR at $T = 50$ K are shown for each sample in Fig. 2 with $B \parallel E$. The characteristic odd-Lorentzian shape is indicative of spins generated in-plane and perpendicular to E [3]. The data are modeled as spins generated along the y direction, with a background subtracted, and are fit to $\theta_{\text{el}}\omega_L\tau/[(\omega_L\tau)^2 + 1]$, where θ_{el} is the KR amplitude, $\omega_L = g\mu_B B/\hbar$ is the Larmor precession frequency, μ_B is the Bohr magneton, and τ is the spin coherence time [3]. We measure θ_{el} to be independent of the square wave frequency and linear with both E and probe power. The trends in τ between samples match the trend in spin coherence time [19], but the values are not numerically identical. For $n = 5 \times 10^{16}$ cm^{-3} and $n = 9 \times 10^{17}$ cm^{-3}, τ decreases with increasing E, but the $n = 9 \times 10^{18}$ cm^{-3} sample exhibits little change in τ. CISP has also been observed in other samples of lower doping density ($n \sim 1 \times 10^{16}$ cm^{-3}), but systematic results are difficult due to large resistivity. Further quantitative optical analysis is performed as in Ref. [3] to estimate the efficiency of the electrical spin generation giving $\theta_{\text{el}} \approx 12$ spins/μm^{-3} at

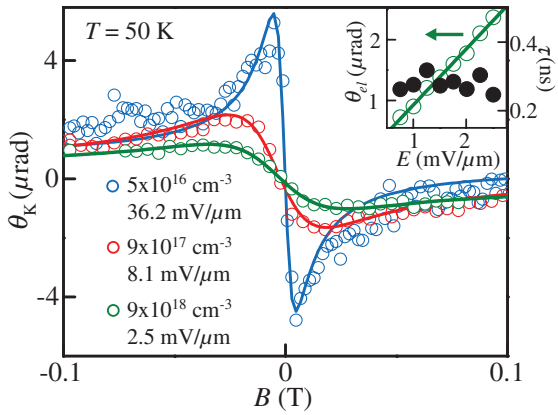

FIG. 2 (color). (a) θ_K as a function of B for n-ZnSe at $T = 50$ K. Open circles are the data, while the solid lines are fits to the data as described in the text. The maximum E that can be applied to each sample without heating decreases with increasing n due to lower sample resistances. The inset shows the electric field dependence of the θ_{el} and τ for the $n = 9 \times 10^{18}$ cm^{-3} sample.

20 K. The sign in the figure corresponds to spins generated along the $+y$ direction when the electric field is in the $+x$ direction.

The microscopic origin of CISP is not well understood [3,23]. In-plane spin generation along the Rashba spin-orbit field [1,24] has been used to explain CISP in two-dimensional electron [25] and hole [26] gases. Following the same formalism, strain-enhanced inversion asymmetry terms in the Hamiltonian manifest as B_{int} and could generate the spin polarization [3,23]. In general, the internal magnetic field strength shows a close correlation to the amount of strain in GaAs structures [2,22], but the magnitude of CISP shows little correlation to the strength of B_{int} [3]. In the current experiment in n-ZnSe, the CISP is comparable in magnitude to that in n-GaAs, even with no observable B_{int}.

The spin Hall effect is probed using a low-temperature scanning Kerr microscope with a spatial resolution of approximately 1 μm [5,7,27]. The ZnSe channel is mounted with $B \perp E$ ($B \parallel y$) so in-plane CISP does not precess and is not detected. No differences in spin accumulation between the [110] and [1$\bar{1}$0] channels are observed. Figure 3(a) shows the geometry for the spin Hall effect measurements, with the laser propagating along $-z$. The origin is taken to be the center of the channel. Figure 3(b) shows typical KR data for scans of B near the edges of the channel at $y = \pm 48$ μm on the $n = 9 \times 10^{18}$ cm^{-3} sample. The KR curves are analogous to the Hanle effect, in which an out-of-plane spin polarization decreases with B due to spin precession [5]; these data can be fit to a Lorentzian $\theta_{\text{el}}/[(\omega_L \tau)^2 + 1]$. The opposite sign of the spin accumulation on each edge of the sample is a signature of the spin Hall effect. This phenomenon is also observed in ZnSe with $n = 8.9 \times 10^{18}$ cm^{-3}, but all of the results presented here are from the sample with $n = 9 \times 10^{18}$ cm^{-3} for brevity. Observation of the spin Hall effect is highly dependent on n doping, as no spin Hall signature is measured in samples with lower n. The growth of higher doped samples is restricted by MBE conditions.

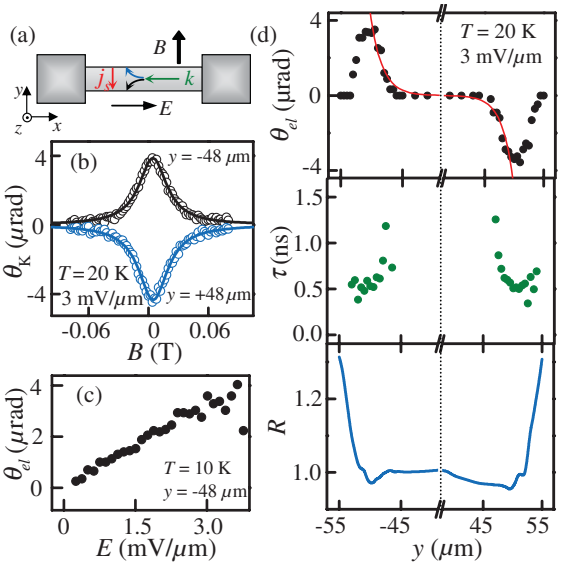

FIG. 3 (color). (a) Schematic showing the measurement geometry for the spin Hall effect, with $B \parallel y$. For $E > 0$, $j_y^s < 0$. (b) θ_K (open circles) and fits (lines) at $x = 0$ μm as a function of B for $y = -48$ μm (black) and $y = +48$ μm (blue) at $T = 20$ K. (c) Electric field dependence of the spin accumulation amplitude θ_{el}. Above $E = 3$ mV/μm, the signal deteriorates due to heating. (d) Spatial dependence of the fit parameters θ_{el} and τ, as well as the reflectivity R of the beam (normalized to 1 at $y = 0$), which is used to monitor the position.

The amplitude of the spin accumulation θ_{el} is linear in E [Fig. 3(c)], while no appreciable change in τ is observed with increasing E. As observed for the spin Hall effect in GaAs, τ increases away from the channel edge [Fig. 3(d)]. The sign and magnitude of the accumulated spins are found by direct comparison to CISP in a geometry with $E \parallel B$, which is calibrated by comparison to time-resolved KR. At 20 K, the peak spin density near the edges is approximated $n_0 \approx 16$ spins/μm^3, with spin polarization along $+z$ ($-z$) on the $y = -50$ μm ($y = +50$ μm) edge for $E > 0$ along x. Assuming a simple spin drift-diffusion model for the accumulation sourced by a spin current, the profile can be fit by $\theta_{\text{el}} = -n_0 \,\text{sech}(w/2L_s) \times \sinh(y/L_s)$ [5,28,29], where L_s is the spin diffusion length [Fig. 3(d)]. These fits give $L_s = 1.9 \pm 0.2$ μm at $T = 20$ K. Ignoring complications arising from boundary conditions, the spin current density along y can be written as $|j_y^s| = L_s n_0/\tau$ [5], and we can calculate the spin Hall conductivity $\sigma_{\text{SH}} = -j_y^s/E_x = 3 \pm 1.5\ \Omega^{-1}\,\text{m}^{-1}/|e|$ at

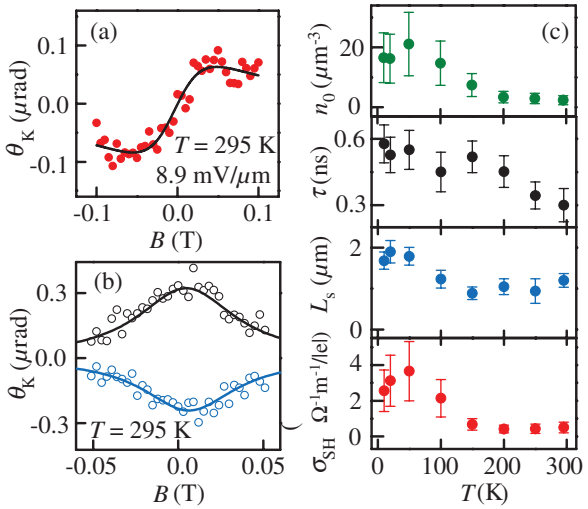

FIG. 4 (color). (a) KR (circles) and fit (line) of CISP at room temperature. Adjacent-point averaging was done to improve the signal-to-noise ratio. (b) KR (circles) and fits (lines) of spin Hall polarization at $y = -48$ μm (black) and $y = +48$ μm (blue) for $T = 295$ K. (c) Temperature dependence of density n_0 (green), coherence time τ (black), spin diffusion length L_s, and spin Hall conductivity σ_{SH}.

$T = 20$ K. Uncertainties in the overall optical calibration make this only an order-of-magnitude estimate.

The spin Hall conductivity for ZnSe is of comparable magnitude and of the same sign as that predicted by theory [10,30] for GaAs with a dominant extrinsic spin Hall effect. The extrinsic spin Hall effect has contributions of differing sign from both skew scattering and the side jump mechanism. For the conditions of Ref. [5], skew scattering likely dominates giving $\sigma_{SH} > 0$. The dominance of skew scattering should persist in the degenerately n-doped ZnSe studied here since the Fermi energy is well above the conduction band edge [30]. Intrinsic spin Hall conductivity should have the opposite sign ($\sigma_{SH} < 0$) [9] and a lower magnitude [10] than measured here; hence, the observed spin Hall effect in ZnSe is likely extrinsic.

Measurements of both CISP and the spin Hall effect at higher temperatures show a decrease in the spin coherence time τ and the peak spin polarization n_0, but both phenomena persist up to room temperature [Figs. 4(a) and 4(b)]. Figure 4(c) shows temperature dependences of the various parameters discussed above. The spin polarization is an order of magnitude weaker at room temperature and L_s decreases from 1.9 μm at 20 K to 1.2 μm at 295 K. The estimated spin Hall conductivity decreases to $\sigma_{SH} \approx 0.5\ \Omega^{-1}\,\mathrm{m}^{-1}/|e|$ at room temperature.

These results demonstrate electrically induced spin polarization and the extrinsic spin Hall effect at room temperature in a II–VI semiconductor. Despite the absence of a measurable internal field and the weaker spin-orbit coupling in ZnSe compared to GaAs, these phenomena remain measurable. The remarkable ability for all-electrical spin generation at room temperature suggests that spin-based logic is technologically feasible in semiconductor devices.

We thank NSF and ONR for financial support. N. P. S. acknowledges the support of the Fannie and John Hertz Foundation.

*Electronic address: awsch@physics.ucsb.edu

[1] A. G. Aronov, Y. B. Lyanda-Geller, and G. E. Pikus, Sov. Phys. JETP **73**, 537 (1991); V. M. Edelstein, Solid State Commun. **73**, 233 (1990).
[2] Y. K. Kato, R. C. Myers, A. C. Gossard, and D. D. Awschalom, Nature (London) **427**, 50 (2004).
[3] Y. K. Kato, R. C. Myers, A. C. Gossard, and D. D. Awschalom, Phys. Rev. Lett. **93**, 176601 (2004).
[4] M. I. Dyakonov and V. I. Perel, Phys. Lett. **35A**, 459 (1971).
[5] Y. K. Kato, R. C. Myers, A. C. Gossard, and D. D. Awschalom, Science **306**, 1910 (2004).
[6] J. Wunderlich, B. Kaestner, J. Sinova, and T. Jungwirth, Phys. Rev. Lett. **94**, 047204 (2005).
[7] V. Sih, R. C. Myers, Y. K. Kato, W. H. Lau, A. C. Gossard, and D. D. Awschalom, Nature Phys. **1**, 31 (2005).
[8] S. Murakami, N. Nagaosa, and S. Zhang, Science **301**, 1348 (2003).
[9] J. Sinova, D. Culcer, Q. Niu, N. A. Sinitsyn, T. Jungwirth, and A. H. MacDonald, Phys. Rev. Lett. **92**, 126603 (2004).
[10] H. Engel, B. I. Halperin, and E. I. Rashba, Phys. Rev. Lett. **95**, 166605 (2005).
[11] J. Shi, P. Zhang, D. Xiao, and Q. Niu, Phys. Rev. Lett. **96**, 076604 (2006).
[12] V. Sih, W. H. Lau, R. C. Myers, V. R. Horowitz, A. C. Gossard, and D. D. Awschalom, Phys. Rev. Lett. **97**, 096605 (2006).
[13] E. M. Hankiewicz, L. W. Molenkamp, T. Jungwirth, and J. Sinova, Phys. Rev. B **70**, 241301(R) (2004); S. I. Erlingsson and D. Loss, Phys. Rev. B **72**, 121310(R) (2005).
[14] S. O. Valenzuela and M. Tinkham, Nature (London) **442**, 176 (2006).
[15] J. M. Kikkawa, I. P. Smorchkova, N. Samarth, and D. D. Awschalom, Science **277**, 1284 (1997); I. Malajovich, J. M. Kikkawa, D. D. Awschalom, J. J. Berry, and N. Samarth, Phys. Rev. Lett. **84**, 1015 (2000).
[16] R. Winkler, *Spin-Orbit Coupling Effects in Two-Dimensional Electron and Hole Systems* (Springer, New York, 2003).
[17] J. Cumings, L. S. Moore, H. T. Chou, K. C. Ku, G. Xiang, S. A. Crooker, N. Samarth, and D. Goldhaber-Gordon, Phys. Rev. Lett. **96**, 196404 (2006).
[18] J. J. Baumberg, S. A. Crooker, D. D. Awschalom, N. Samarth, H. Luo, and J. K. Furdyna, Phys. Rev. B **50**, 7689 (1994).
[19] I. Malajovich, J. M. Kikkawa, D. D. Awschalom, J. J. Berry, and N. Samarth, J. Appl. Phys. **87**, 5073 (2000).
[20] J. M. Kikkawa and D. D. Awschalom, Nature (London) **397**, 139 (1999).
[21] S. A. Crooker and D. L. Smith, Phys. Rev. Lett. **94**, 236601 (2005).
[22] V. Sih, H. Knotz, J. Stephens, V. R. Horowitz, A. C. Gossard, and D. D. Awschalom, Phys. Rev. B **73**, 241316(R) (2006).
[23] B. Andrei Bernevig and Shou-Cheng Zhang, Phys. Rev. B **72**, 115204 (2005).
[24] D. Culcer, Y. Yao, A. H. MacDonald, and Q. Niu, Phys. Rev. B **72**, 045215 (2005).
[25] C. L. Yang, H. T. He, Lu Ding, L. J. Cui, Y. P. Zeng, J. N. Wang, and W. K. Ge, Phys. Rev. Lett. **96**, 186605 (2006).
[26] A. Yu. Silov, P. A. Blajnov, J. H. Wolter, R. Hey, K. H. Ploog, and N. S. Averkiev, Appl. Phys. Lett. **85**, 5929 (2004).
[27] J. Stephens, R. K. Kawakami, J. Berezovsky, M. Hanson, D. P. Shepherd, A. C. Gossard, and D. D. Awschalom, Phys. Rev. B **68**, 041307(R) (2003).
[28] S. Zhang, Phys. Rev. Lett. **85**, 393 (2000).
[29] W. Tse, J. Fabian, I. Zuric, and S. Das Sarma, Phys. Rev. B **72**, 241303(R) (2005).
[30] W. Tse and S. Das Sarma, Phys. Rev. Lett. **96**, 056601 (2006).